






Interplay between magnetic and lattice excitations and emergent multiple phase transitions in $\text{MnPSe}_{3-x}\text{S}_x$

Deepu Kumar ¹, Nguyen The Hoang ¹, Yumin Sim,¹ Youngsu Choi ², Kalaivanan Raju,³ Rajesh Kumar Ulaganathan ³, Raman Sankar,³ Maeng-Je Seong,^{1,*} and Kwang-Yong Choi ^{2,†}

¹*Department of Physics and Center for Berry Curvature-based New Phenomena (BeCaP),*

Chung-Ang University, Seoul 06974, Republic of Korea

²*Department of Physics, Sungkyunkwan University, Suwon 16419, Republic of Korea*

³*Institute of Physics, Academia Sinica, Taipei 10617, Taiwan*



(Received 15 April 2024; revised 24 July 2024; accepted 25 July 2024; published 12 August 2024)

The intricate interplay between spin and lattice degrees of freedom in two-dimensional magnetic materials plays a pivotal role in modifying their magnetic characteristics, engendering hybrid quasiparticles, and implementing functional devices. Herein, we present our comprehensive and in-depth investigations on magnetic and lattice excitations of $\text{MnPSe}_{3-x}\text{S}_x$ ($x = 0, 0.63$, and 1.68) alloys, utilizing temperature- and polarization-dependent Raman scattering. Our experimental results reveal the occurrence of multiple phase transitions, evidenced by notable changes in phonon self-energy and the appearance or splitting of phonon modes. These emergent phases are tied to the development of long and short-range spin-spin correlations, as well as to spin reorientations or magnetic instabilities. Our analysis of two-magnon excitations as a function of temperature and composition showcases their hybridization with phonons whose degree weakens with increasing x . Moreover, the suppression of spin-dependent phonon intensity in chemically most-disordered $\text{MnPSe}_{3-x}\text{S}_x$ ($x = 1.68$) suggests that chalcogen substitution offers a control knob of tuning spin and phonon dynamics by modulating concurrently superexchange pathways and a degree of trigonal distortions.

DOI: [10.1103/PhysRevB.110.064414](https://doi.org/10.1103/PhysRevB.110.064414)

I. INTRODUCTION

The quest for two-dimensional (2D) magnetism in van der Waals (vdW) materials constitutes an exciting frontier in condensed-matter physics, especially in the context of the Mermin-Wagner theorem, which negates the possibility of long-range ordering at finite temperatures in 2D systems with isotropic interactions [1]. However, the discovery of long-range magnetic order in vdW materials such as CrI_3 [2] and $\text{Cr}_2\text{Ge}_2\text{Te}_6$ [3] has expanded the purview of low-dimensional magnetism and catalyzed extensive research into magnetism at the 2D limit, subsequently enlarging the family of 2D magnetic materials [4,5].

Among these materials, transition-metal phosphorous trichalcogenides MPX_3 ($M = \text{Mn, Fe, Ni, V, Co}$; $X = \text{S, Se}$), which form vdW antiferromagnets (AFMs), have emerged as exceptional platforms for exploring the exotic and topological properties of 2D magnetism [6–11]. Singularly, the magnetic exchange interactions, spin ordering patterns, spin dimensionality, and magnetic anisotropies are strongly dependent on the specific choice of M or X atoms. For example, NiPS_3 is characterized by an XXZ -type AFM ($T_N \sim 155$ K) with zigzag-ordered moments lying in the ab plane, while FePS_3 embodies an Ising AFM with an out-of-plane zigzag order at $T_N \sim 123$ K [10,12]. The Heisenberg AFM MnPS_3 undergoes a transition

to Néel-type ordering at $T_N \sim 78$ K. Conversely, its selenium counterpart MnPSe_3 exhibits large XY anisotropy with a similar ordering temperature of $T_N \sim 74$ K [13]. Additionally, the spin ordering orientation relies on the species of nonmagnetic ions; in MnPSe_3 , the spins are aligned within the ab plane, whereas in MnPS_3 , the ordered magnetic moments lie perpendicular to the ab plane. The distinct magnetic anisotropies and interactions observed in MnPX_3 are discussed in terms of the combined effects of trigonal distortion of the MnX_6 octahedra and spin-orbit coupling [13,14], highlighting the tunability of magnetic properties through chemical substitution.

In this vein, the variation among magnetic or nonmagnetic atoms can lead to the emergence of exotic magnetic phenomena in alloyed compounds, $\text{MM}'\text{PX}_3$ (M and M' represent different transition-metal atoms) or $\text{MP}(\text{XX}')_3$ (X and X' are different chalcogen atoms). This is owed to the interplay between competing magnetic interactions of heterogeneous magnetic ions, varying strengths of spin-orbit coupling between magnetic and chalcogen atoms, and magnetic anisotropy. A wide spectrum of studies focusing on alloying at the M site, including $\text{Ni}_{1-x}\text{Fe}_x\text{PS}_3$, $\text{Ni}_{1-x}\text{Mn}_x\text{PS}_3$, $\text{Mn}_{1-x}\text{Fe}_x\text{PSe}_3$, $\text{Mn}_x\text{Zn}_{1-x}\text{PS}_3$, $\text{Ni}_{1-x}\text{Co}_x\text{PS}_3$, and $\text{Fe}_{1-x}\text{Zn}_x\text{PS}_3$ etc., has showcased the intriguing and remarkable properties of these alloyed states [11,14–21]. Moreover, substituting nonmagnetic chalcogen atoms, as in $\text{MP}(\text{XX}')_3$, is expected to fine-tune magnetism through changes in the crystal-field splitting of the MX_6 octahedra and spin-orbit coupling. Although most research to date has concentrated on mixed $\text{MM}'\text{PX}_3$ compounds or end members,

*Contact author: mseong@cau.ac.kr

†Contact author: choisky99@skku.edu

the study of magnetic properties associated with chalcogen-substitution in $MP(XX')_3$ mixed compounds has received relatively little attention. Recent research on chalcogen-substituted $MP(XX')_3$ compounds, specifically $MnPS_{3-x}Se_x$, and $NiPS_{3-x}Se_x$ by Basnet *et al.* [22] and $MnPS_{3(1-x)}Se_{3x}$ by Han *et al.* [23], has demonstrated remarkable alterations in the magnetic properties of these mixed alloyed compounds, as evidenced by magnetic susceptibility measurements.

In addition to diverse static magnetic behaviors, the class of MPX_3 material exhibits a variety of quasiparticle excitations, such as magnetic, excitonic, and lattice excitations, along with their mutual interactions. Notable phenomena observed in MPX_3 compounds encompass both low-energy and high-energy magnetic excitations, strong magnon-phonon coupling, and coupled magnon-phonon modes, generally known as magnon-polarons [24–28]. Given this, a thorough comprehension of magnon dynamics and its coupling to lattices is essential not only for fundamental research but also for implementing low-energy consumption technologies in magnonic devices. Despite this significance, only room-temperature Raman-scattering measurements for $MnPS_{3-x}S_x$ [29] have been conducted, with a lack of detailed temperature-dependent Raman studies. Temperature-dependent Raman scattering has been proven to be a powerful and nondestructive technique to investigate not only lattice vibrations but also various quasiparticle excitations inherent to 2D MPX_3 magnetic materials [24,30–32].

In this work, we present a comprehensive temperature- and polarization-dependent Raman study to decipher the impact of chalcogen substitution on the magnetic behaviors in $MnPS_{3-x}S_x$ ($x = 0.0, 0.63, \text{ and } 1.68$) compounds. We observe an additional phase transition within the long-ranged ordered phase, evident through phonon anomalies and supported by magnetic susceptibility data. This subtle transition is likely linked to spin reorientations arising from additional trigonal distortions of the MnX_6 octahedra, facilitated by spin-lattice couplings. In $MnPS_{3-x}S_x$ ($x = 1.68$) with near-maximum chemical disorder, we find that the hybridized character of two-magnon excitations and spin-dependent Raman scatterings weaken due to the presence of competing exchange interactions, highlighting the tunability of magnetic properties through chalcogen substitution.

II. EXPERIMENTAL DETAILS

Single crystals of $MnPS_{3-x}S_x$ ($x = 0, 0.63, \text{ and } 1.68$) were grown using the chemical vapor transport method with iodine as the transport agent. Initially, polycrystalline powders were prepared by the solid-state reaction process. The stoichiometry 3N purity of a selenium slug (Se), phosphorus powder (P), sulfur powder (S), and manganese powders (Mn) were added into a quartz ampoule and sealed under high-vacuum conditions. The mixtures were sintered at 400 and 600 °C, with intermediate grinding to prepare the single phase of the compounds. For crystal growth, 200 mg of iodine was added to the synthesized powders in a quartz ampoule of 350 mm in length, and sealed under high-vacuum conditions. The tube was kept in a horizontal two-zone furnace and maintained at constant temperatures of 700 and 600 °C for 200 h. After the growth process was completed, the

furnace temperature was cooled to room temperature at a rate of 2 °C/min. Finally, high-quality layered single crystals were collected from the cold end of the tubes.

Raman-scattering measurements were done using the Princeton SpectraPro HRS-750 spectrometer in backscattering geometry. A 532 nm (2.33 eV) laser was used to excite the Raman spectrum. A laser was kept at a low power of $\sim 300 \mu\text{W}$ to avoid any local heating and damage to the sample. The incident laser beam was focused on the sample using a $50\times$ objective lens, which was also used to collect the scattered light from the sample. The scattered light was detected using a 1200 grating coupled with an electrically cooled BLAZE charge coupled device detector. Temperature-dependent Raman measurements were carried out using a closed-cycle cryostat (Montana Cryostat) by varying the temperature from 3.5 to 330 K with a temperature accuracy of ± 0.1 K. A waiting time of ~ 10 min was kept after each Raman measurement to ensure temperature stability. The phase purity and stoichiometry of the single crystals were checked by x-ray diffraction and energy-dispersive x-ray spectroscopy (EDX); see Figs. S2 and S3 in Supplemental Material for details [33].

A set of linear polarizer–quarter-wave plates was used to perform polarization-dependent Raman measurements. A vertical analyzer (polarizer) was installed in front of the spectrometer to keep the signal constant with respect to the grating orientation. Two quarter-wave plates were utilized: one in the path of incident light and the other in the path of scattered light, to achieve right or left circularly polarized light. The quarter-wave plate in the incident light beam path was adjusted to maintain the helicity of the incident beam on the sample as right (σ^+) circularly polarized and was kept fixed. The quarter-wave plate in the scattered light beam path was rotated to obtain the helicity of the scattered light beam as either left (σ^-) or right (σ^+), resulting in cocircular ($\sigma^+\sigma^+$) and cross-circular ($\sigma^+\sigma^-$) polarized configurations.

Temperature-dependent magnetic susceptibility measurements were carried out using a superconducting quantum interference device vibrating sample magnetometer (Quantum Design) with an externally applied magnetic field of $\mu_0 H = 0.02$ T.

To extract the frequency, full width at half maximum (FWHM), and intensity of the phonon modes, Raman spectra were fitted using the sum of the Lorentzian functions built in the ORIGIN software, which is expressed as $S(\omega) = S_0(\omega) + \sum_i \frac{2A_i}{\pi} \frac{\Gamma_i}{4(\omega - \omega_i)^2 + \Gamma_i^2}$, where A_i , ω_i , and Γ_i are the intensity, frequency, and FWHM of the phonon modes, respectively. After making baseline correction and selecting the number of peaks to be fitted, we ran the iteration until we achieved the best fit of the spectrum.

III. RESULTS AND DISCUSSION

A. Raman scattering in $MnPS_{3-x}S_x$

1. Phonon excitations in $MnPS_{3-x}S_x$

Figure 1(a) shows the unpolarized Raman spectrum of bulk $MnPS_{3-x}S_x$ in a spectral range of 30–650 cm^{-1} , collected at a temperature of $T = 3.5$ K. Section S1 of the Supplemental Material [33] provides information about the crystal and magnetic structures, while Sec. S2 provides further

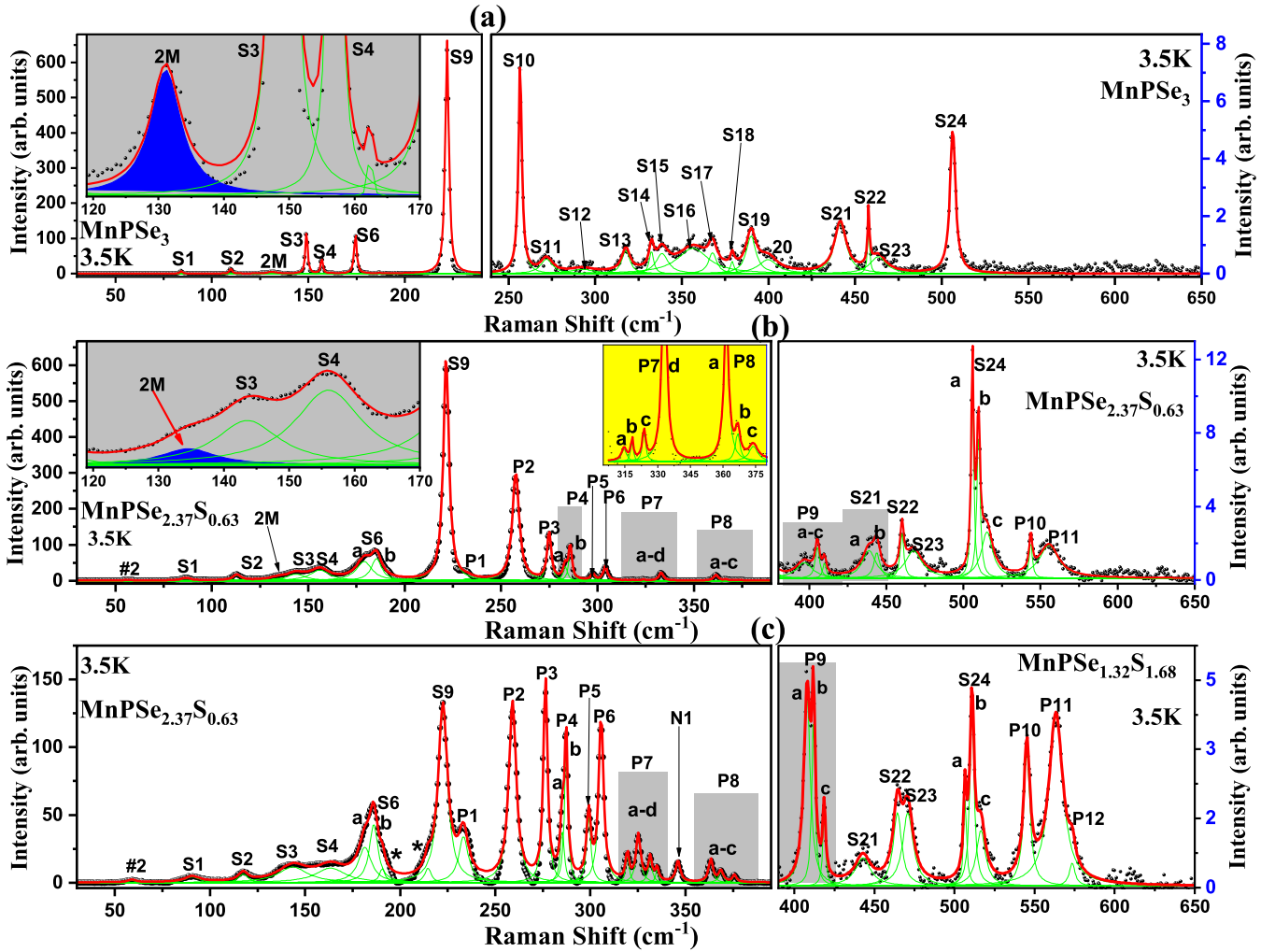


FIG. 1. Unpolarized Raman spectrum of (a) MnPSe_3 , (b) $\text{MnPSe}_{2.37}\text{S}_{0.63}$, and (c) $\text{MnPSe}_{1.32}\text{S}_{1.68}$ in the spectral range of 30–650 cm^{-1} collected at 3.5 K. The solid red line shows the total sum of Lorentzian fit, and the thin green lines show the individual fits of the Raman features. The observed phonon modes are labeled as S1–S24, P1–P10, and N1. Insets (a) and (b) in gray are the amplified spectrum for the spectral range of 120–170 cm^{-1} . The observed peak (blue shaded) is attributed to the two-magnon (2M) excitations. For the case of $\text{MnPSe}_{1.32}\text{S}_{1.68}$, the two-magnon signal is not clearly visible due to very close to intense and broad S3 mode. Inset (b) in yellow is the amplified spectrum for the spectral range of 305–380 cm^{-1} .

information about the expected phonons at the Brillouin-zone center for both MnPSe_3 and MnPS_3 ; see Supplemental Material [33]. The observed modes are labeled as S1–S24 for convenience and listed in Table S1 (Supplemental Material [33]), along with their frequency and symmetry assignments based on previous studies [24,31,34,35], and our circularly polarized Raman measurements; the circularly polarized Raman spectrum collected at 3.5 K is shown in Fig S4 [33].

In the Raman spectrum of MPX_3 materials, despite their complex unit cell, phonons are broadly classified into two categories: (i) external phonons, which are mainly associated with the vibrations of magnetic transition-metal atom (M) and lie in the low-frequency range of Raman spectrum, and (ii) internal phonons, which involve symmetric stretching of the P–X and P–P bonds within the $(\text{P}_2\text{X}_6)^{4-}$ cluster and are typically situated in the high spectral frequency range. The cutoff frequency that divides the high- and low-frequency regimes varies with the specific M or X atoms. Experimentally,

for the case of MnPSe_3 and MnPS_3 , the low-frequency spectral range is expected to be below 140 and 200 cm^{-1} , respectively. For MnPSe_3 , we observed six modes: S1 (E_g) and S2 (E_g) correspond to the vibrations of Mn^{2+} ions, and S3 (A_g), S4 (E_g), S6 (E_g), and S9 (A_g) are associated with the vibrations of the nonmagnetic $(\text{P}_2\text{Se}_6)^{4-}$ cluster. These six peaks have been previously reported in previous Raman studies for MnPSe_3 in the frequency range of 70–240 cm^{-1} [24,31,34,35]. Additionally, the broad maximum peaking at 131.1 cm^{-1} [marked by the blue shading in the inset of Fig. 1(a)] is attributed to two-magnon (2M) excitations, being in line with earlier Raman studies [24].

Circularly polarized Raman measurements reveal the E_g character of 2M excitation through its appearance in a cross-circularly polarized configuration. Upon warming, it softens and broadens significantly, first hybridizing with S2 mode around 50–55 K and then with S1 around T_N , which will be discussed in more detail later. At low temperatures, three

additional weak Raman modes $S5$ at ~ 162.2 cm^{-1} , $S7$ at ~ 186.7 cm^{-1} , and $S8$ at ~ 195.6 cm^{-1} vanish near or above T_N , as shown in Fig. S7(a); see Supplemental Material [33]. We assign these A_g modes to magnetically driven activated phonons. It is noteworthy that MnPS_3 and MnPSe_3 have identical magnetic and crystallographic units, ruling out the possibility of zone-folded phonons due to no folding of the Brillouin zone [36]. Furthermore, no structural changes have been reported for MnPSe_3 [8], suggesting that the appearance of these modes could not be attributed to Brillouin-zone folding or structural changes. Since these phonons appear below T_N , magnetoelastic couplings may be responsible for the $S5$, $S7$, and $S8$ peaks.

The right panel of Fig. 1(a) shows the Raman spectrum of MnPSe_3 in a spectral range of 240–650 cm^{-1} . The peak $S10$, assigned to an A_g symmetry, appears narrower than in previous studies, which reported a relatively broader peak at this frequency [37]. We further note that the peak $S10$ is more intense compared to other modes observed in the 240–650- cm^{-1} range. A group of phonons, $S11$ – $S20$, is in line with the previous study [37], which become unidentifiable or weaken above T_N ; see Fig. S6 [33]. The observed modes $S22$ (E_g) and $S24$ (A_g) are consistent with those identified in both theoretical and experimental studies [24,38]. $S24$ may be related to the P-P stretching vibrational mode because this mode was reported at around 500 cm^{-1} in Se-based compounds, while the same mode has been observed at around 600 cm^{-1} in S-based compounds. This indicates that the frequency of this mode is independent of the M atoms, yet strongly dependent on the $(\text{P}_2\text{X}_6)^{4-}$ [36,38]. A broad and weak $S21$ (A_g) mode around 440 cm^{-1} appears to be an overtone of the intense $S9$ mode, consistent with the selection rule of second-order Raman scattering. Generically, second-order phonons are broader and weaker than the corresponding first-order phonons. The intensity of the n th-order modes is generally governed by g^n , except for resonant scatterings. Here, n is an order of phonon scatterings and g is the electron-phonon coupling parameter, which is less than one. Therefore, the intensity of higher-order modes is expected to decrease as n increases. From Fig. 1(a), it is evident that the $S21$ is nearly doubled in the frequency of $S9$, significantly weaker and broader.

2. Phonon excitations in $\text{MnPSe}_{3-x}\text{S}_x$ ($x = 0.63$ and 1.68)

Figures 1(b) and 1(c) present the unpolarized Raman spectra of $\text{MnPSe}_{2.37}\text{S}_{0.63}$ and $\text{MnPSe}_{1.32}\text{S}_{1.68}$ in a spectral range of 30–650 cm^{-1} , collected at 3.5 K, respectively. Surprisingly, distinct changes are observed in these mixed compounds compared to the parent MnPSe_3 . The most noticeable differences in phonon modes between MnPSe_3 and the mixed $\text{MnPSe}_{2.37}\text{S}_{0.63}$ and $\text{MnPSe}_{1.32}\text{S}_{1.68}$ compounds are (i) the linewidth broadening and (ii) the emergence or splitting of certain phonon modes. Specifically, for $\text{MnPSe}_{2.37}\text{S}_{0.63}$ ($\text{MnPSe}_{1.32}\text{S}_{1.68}$) the $S1$ and $S2$ modes broaden by ~ 4 (7.5) and ~ 3 (3.5) cm^{-1} , respectively, compared to those of MnPSe_3 . Similar to $S1$ and $S2$, a significant broadening is observed for the $S3$, $S4$, and $S6$ modes in the mixed compounds compared to those of MnPSe_3 . Interestingly, the $S6$ mode not only broadens but also splits into two distinct phonon

modes, namely $S6a$ and $S6b$, demonstrating orthogonal behavior under circularly polarized Raman measurements. More specifically, the $S6a$ mode is present in $\sigma^+\sigma^-$ polarization, while the $S6b$ mode is seen in $\sigma^+\sigma^+$ configurations, indicating E_g and A_g symmetries, respectively; see Figs. 1(b) and 1(c), and Figs. S4(b) and S4(c) in the Supplemental Material [33].

The mode $S24$ in MnPSe_3 splits into three modes: $a \sim 505.9$, $b \sim 509.8$, and $c \sim 515.3$ cm^{-1} for $\text{MnPSe}_{2.37}\text{S}_{0.63}$ and $a \sim 506.6$, $b \sim 510.9$, and $c \sim 516.5$ cm^{-1} for $\text{MnPSe}_{1.32}\text{S}_{1.68}$. For $\text{MnPSe}_{2.37}\text{S}_{0.63}$, this splitting persists up to 210 K, while for $\text{MnPSe}_{1.32}\text{S}_{1.68}$, the splitting of $S24$ modes is observed up to only ~ 150 K; see Figs. 2(c) and 2(f). Surprisingly, the splitting-energy differences between the a and b modes and between the b and c modes are identical, $\Delta\omega_{S24(b-a)} \sim 4$ cm^{-1} and $\Delta\omega_{S24(c-b)} \sim 5.5$ cm^{-1} for both $\text{MnPSe}_{2.37}\text{S}_{0.63}$ and $\text{MnPSe}_{1.32}\text{S}_{1.68}$. The average frequency is found to be nearly identical: $\omega_{\text{avg}} \sim 510.3$ cm^{-1} for $\text{MnPSe}_{2.37}\text{S}_{0.63}$ and $\omega_{\text{avg}} \sim 511.3$ cm^{-1} for $\text{MnPSe}_{1.32}\text{S}_{1.68}$, but ~ 4 – 5 cm^{-1} larger than that of the $S24$ mode in MnPSe_3 . Notably, $S24a$ is more intense than $S24b$ for $\text{MnPSe}_{2.37}\text{S}_{0.63}$ while $S24b$ is more intense than $S24a$ for $\text{MnPSe}_{1.32}\text{S}_{1.68}$. Furthermore, all split components of $S24$ are observed in $\sigma^+\sigma^+$ configuration, suggesting A_g symmetry.

As mentioned before, the splitting of the $S24$ peak, associated with the P-P stretching vibrational mode, is questionable, given its persistence into the phase of short-ranged spin-spin correlations or even beyond the short-ranged phase. Considering the splitting is observed exclusively in the mixed compounds, it may be related to several factors: (i) magnetic (stacking) disorder-induced symmetry breaking because the end compounds show different stacking orders and magnetic structures, and (ii) Brillouin zone folding. Since no Brillouin-zone folding and thus no zone-folded phonons are expected in the parent MnPSe_3 and MnPS_3 compounds, the observed phenomenon in the mixed compounds suggests that Brillouin-zone folding, due to the differing crystal symmetries of the end members, might activate zone-boundary phonons. Thus, the pronounced splitting of the $S24$ mode in the mixed compounds is probably linked to either the zone-folding phenomena or magnetic (stacking) disorder-induced symmetry breaking.

Additionally, we observed additional phonon modes in the mixed $\text{MnPSe}_{2.37}\text{S}_{0.63}$ and $\text{MnPSe}_{1.32}\text{S}_{1.68}$ compounds, labeled $P1$, $P2$, ..., $P12$, and $N1$ and listed in Table S1 in the Supplemental Material [33]. These phonon modes could be related to those of the parent MnPS_3 or arise due to local structural distortions in these mixed compounds. Furthermore, we also observe several very weak shoulder modes near intense peaks, marked by an asterisk in Fig. 1(c). The modes $P1$ at ~ 232 cm^{-1} , $P2$ at ~ 257.6 cm^{-1} , and $P3$ at ~ 274.9 cm^{-1} closely match the characteristic Raman features of the bulk MnPS_3 with B_g/A_g , A_g , and B_g/A_g symmetry, respectively, attributed to the vibration of the $(\text{P}_2\text{S}_6)^{4-}$ cluster [39,40]. We note that the selection rule allows A_g mode in cocircular- and B_g mode in cross-circular polarized configurations; see Sec. S3 in the Supplemental Material [33] for more details. We further note that the pairs of quasidegenerate A_g and B_g modes possess a symmetry similar to E_g , as found in phonons around

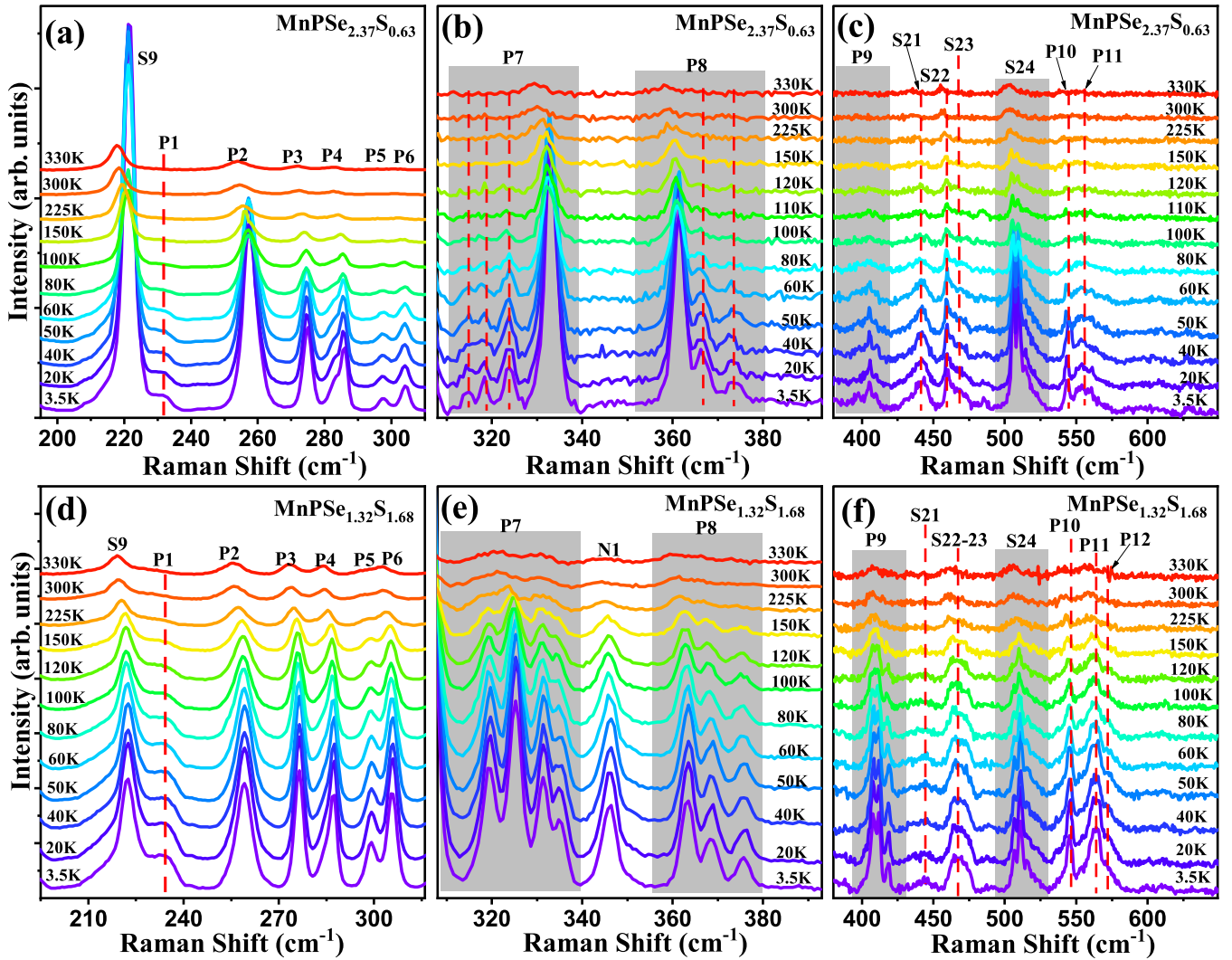


FIG. 2. (a), (b), and (c) Temperature evolution of the unpolarized Raman spectrum of $\text{MnPSe}_{2.37}\text{S}_{0.63}$ in the frequency range of 190–310, 310–390, and 380–650 cm^{-1} , respectively. (d), (e), and (f) Temperature evolution of the Raman spectrum of $\text{MnPSe}_{1.32}\text{S}_{1.68}$ in a frequency range of 190–310, 310–390, and 380–650 cm^{-1} , respectively.

220–230 cm^{-1} in MnPS_3 [39]. In our case, $P1$ is observed in cross-circular polarization, akin to the E_g mode, indicating that $P1$ is indeed related to the B_g/A_g mode of MnPS_3 . On the other hand, $P3$, observed in cocircular configuration, is in stark contrast with a peak around 275 cm^{-1} , as is reported in cross-circular configurations for MnPS_3 [39]. $\text{MnPSe}_{1.32}\text{S}_{1.68}$ shows a broad mode marked by $N1$ entered at 346.1 cm^{-1} , which is absent for $\text{MnPSe}_{2.37}\text{S}_{0.63}$.

In the spectral range of 310–390 cm^{-1} , the $P7$ and $P8$ modes are grouped into four and three peaks, respectively. For $\text{MnPSe}_{2.37}\text{S}_{0.63}$, the lower-side modes of $P7a$, $P7b$, and $P7c$ are weaker by an order of magnitude than the $P7d$ mode. On the other hand, the $P8b$ and $P8c$ modes are almost 5 times less intense than the $P8a$ mode. Noticeably, these two $P7$ and $P8$ groups become nearly identically intense for the case of $\text{MnPSe}_{1.32}\text{S}_{1.68}$; see Figs. 1(b) and 1(c). Furthermore, for $\text{MnPSe}_{2.37}\text{S}_{0.63}$, $P7a$ – $P7c$ and $P8b$ and $P8c$ are discernible below T_N ; see Fig. 2(b). For $\text{MnPSe}_{1.32}\text{S}_{1.68}$, on the other hand, most of the grouped $P7$ and $P8$ modes (with a few exceptions)

are observed up to our highest recorded temperature; see Fig. 2(e), and Fig. S13 in the Supplemental Material [33].

In addition to the $P7$ and $P8$ grouped phonons, we further observe $P9$, a group of three modes in the spectral 395–425 cm^{-1} in both $\text{MnPSe}_{2.37}\text{S}_{0.63}$ and $\text{MnPSe}_{1.32}\text{S}_{1.68}$ compounds. These $P9$ phonons are more intense in $\text{MnPSe}_{1.32}\text{S}_{1.68}$ than in $\text{MnPSe}_{2.37}\text{S}_{0.63}$. With the temperature rises, for $\text{MnPSe}_{2.37}\text{S}_{0.63}$, the $P9$ peaks merge into a broad single peak around 70–80 K and disappear above 150–160 K. For the case of $\text{MnPSe}_{1.32}\text{S}_{1.68}$, the split components of $P9$ are pronounced at low temperatures, and a single peak is observed up to our highest recorded temperature; see Figs. 2(c) and 2(f), and Fig. S13 in the Supplemental Material [33]. Finally, we observe two ($P10$ and $P11$) and three ($P10$ – $P12$) peaks in the spectral range of 525–600 cm^{-1} for $\text{MnPSe}_{2.37}\text{S}_{0.63}$ and $\text{MnPSe}_{1.32}\text{S}_{1.68}$, respectively, corresponding to the high-frequency phonon modes of MnPS_3 [38–40].

The appearance of extra phonon peaks, typical for alloyed MPX_3 compounds [21,41], may be attributed to multiple

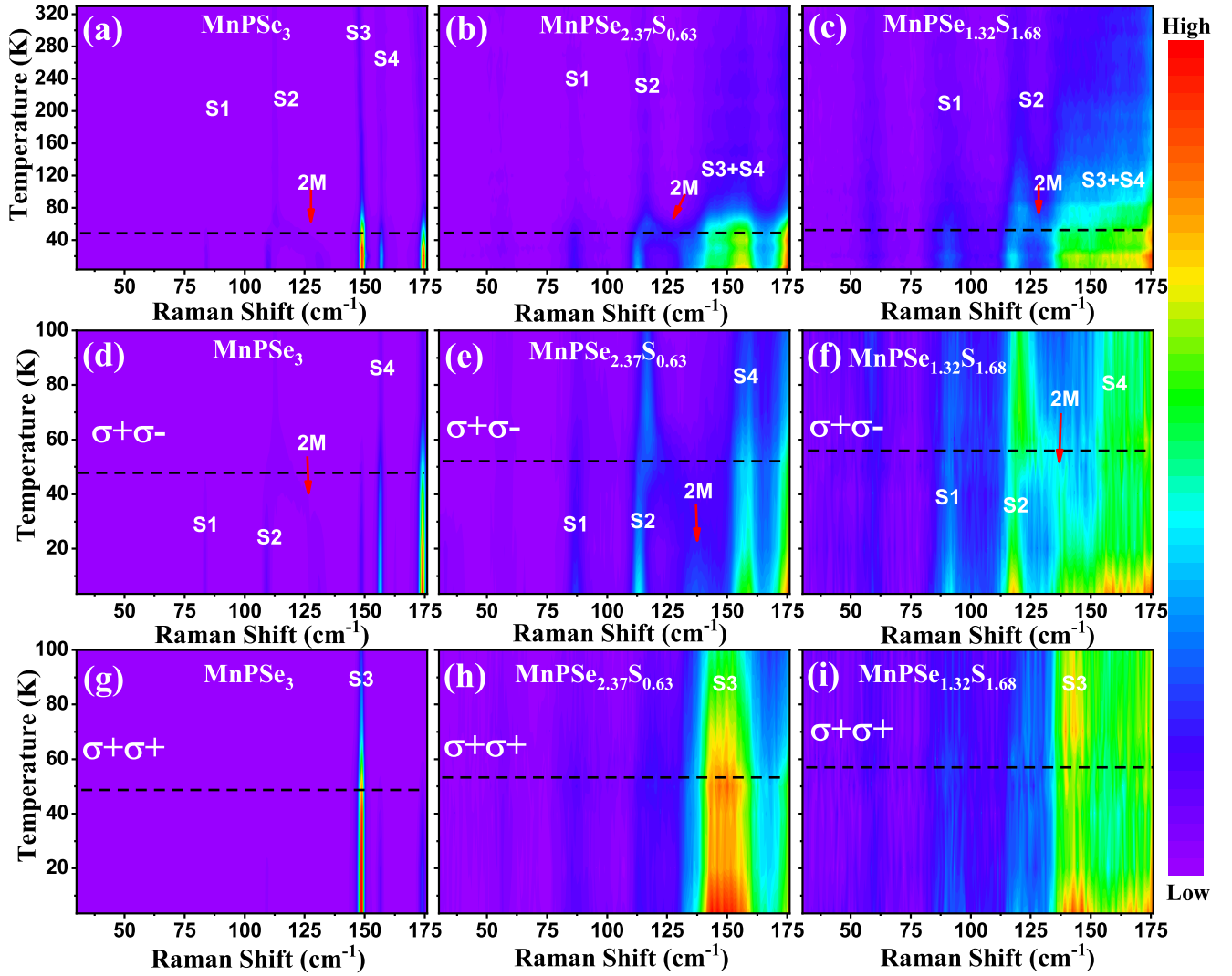


FIG. 3. Unpolarized 2D color contour maps of the Raman intensity vs Raman shift and as a function of temperature (3.5–330 K) for (a) MnPSe_3 , (b) $\text{MnPSe}_{2.37}\text{S}_{0.63}$, and (c) $\text{MnPSe}_{1.32}\text{S}_{1.68}$ in a frequency range of 30–175 cm^{-1} . Two-dimensional color contour maps of the Raman intensity vs Raman shift and as a function of temperature (3.5–100 K) for (d) MnPSe_3 , (e) $\text{MnPSe}_{2.37}\text{S}_{0.63}$, and (f) $\text{MnPSe}_{1.32}\text{S}_{1.68}$ collected cross-circularly ($\sigma^+\sigma^-$); (g) MnPSe_3 , (h) $\text{MnPSe}_{2.37}\text{S}_{0.63}$ and (i) $\text{MnPSe}_{1.32}\text{S}_{1.68}$ collected in cocircularly ($\sigma^+\sigma^+$) polarized configuration in a frequency range of 30–175 cm^{-1} . Two-magnon signal is marked by a red arrow. The horizontal black dashed line indicates the magnon-phonon hybridization temperature.

factors: (i) spin-spin and spin-phonon coupling, (ii) Brillouin-zone folding, (iii) changes in local structural distortions or symmetry breaking, and (iv) quantum interference between discrete phononic state and the electronic excitations due to spin splitting in the band structure [21,41–44]. To simplify the presentation and avoid confusion, from now on, we will use our simple phonon-mode notation, unless symmetry of phonon mode is required; see Table S1 for the symmetry assignments of the modes.

B. Two-magnon Raman scattering

Now, we turn to 2M excitations and their temperature and composition dependence. In antiferromagnets, 2M Raman scattering occurs through the excitations of two magnons with equal but opposite momentum [45,46]. Since the 2M scattering processes are dictated by the

exchange-scattering mechanism [46–48], its scattering intensity can be much stronger than the one-magnon one, bearing information about spin dynamics and magnetic exchange interactions.

Figures 3(a)–3(c) show the unpolarized 2D color contour maps of the Raman intensity versus Raman shift across a temperature range of 3.5–330 K for (a) MnPSe_3 , (b) $\text{MnPSe}_{2.37}\text{S}_{0.63}$, and (c) $\text{MnPSe}_{1.32}\text{S}_{1.68}$ in a frequency range of 30–175 cm^{-1} and see Figs. S8 (a-c) in the Supplemental Material [33] in a frequency and temperature range of 60–140 cm^{-1} and 3.5–150 K for clear visibility of 2M signal, respectively. The 2M excitation is marked by a red arrow. In the unpolarized Raman spectrum of MnPSe_3 , the 2M feature is well resolved and separated from phonon modes at the lowest recorded temperature, while it appears as a sideband in $\text{MnPSe}_{2.37}\text{S}_{0.63}$. On the other hand, the 2M overlaps with phonons for $\text{MnPSe}_{1.32}\text{S}_{1.68}$; see Fig. 3(c). Notably,

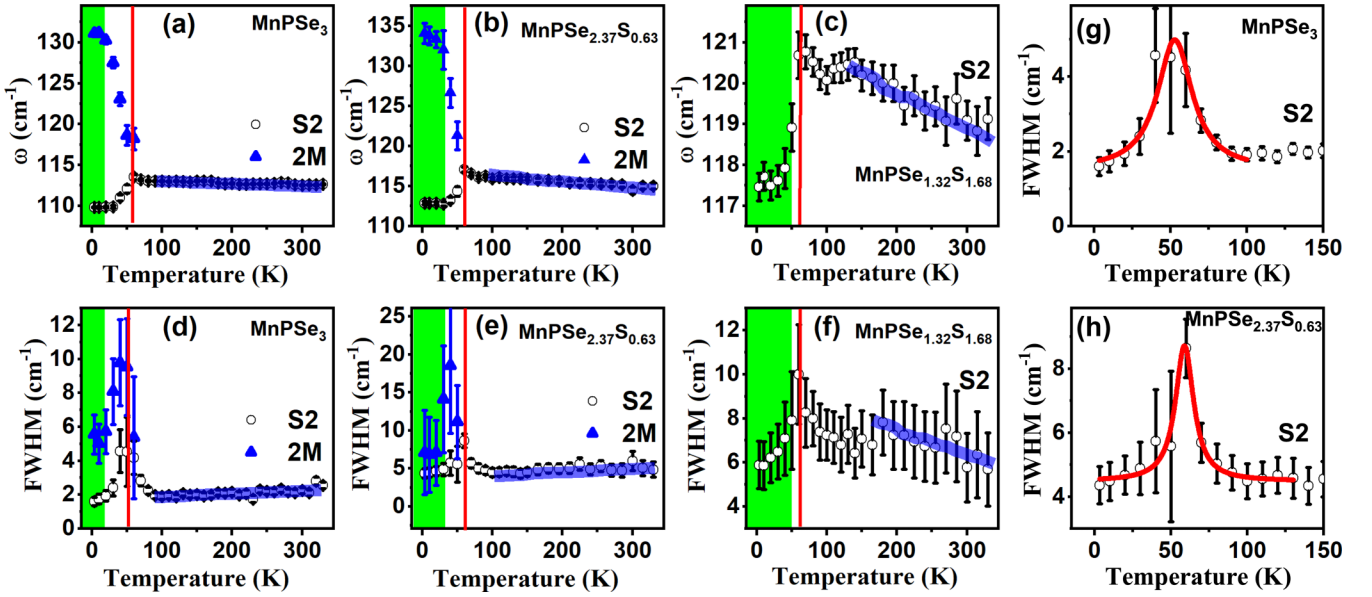


FIG. 4. (a), (b), and (c) Temperature-dependent frequency of $S2$, and $2M$ for MnPS_3 , $\text{MnPSe}_{2.37}\text{S}_{0.63}$, and $\text{MnPSe}_{1.32}\text{S}_{1.68}$, respectively. (d), (e), and (f) Temperature-dependent FWHM of $S2$, and $2M$ for MnPS_3 , $\text{MnPSe}_{2.37}\text{S}_{0.63}$, and $\text{MnPSe}_{1.32}\text{S}_{1.68}$, respectively. A solid vertical red line around 50–60 indicates the hybridization of $2M$ with $S2$ (E_g). (g), (h) Temperature-dependent FWHM of $S2$ in the temperature range of 3.5 to 150 K for MnPS_3 and $\text{MnPSe}_{2.37}\text{S}_{0.63}$, plotted for clear visibility, respectively. The green shaded area shows the topological phase region ($T1$). Solid red curves in (g) and (h) are the fits using the Lorentzian function. Semitransparent blue lines are guides to the eye. The error bars are the standard error, and were obtained during the extraction of the self-energy parameters using Lorentzian fitting.

the existence of the $2M$ excitations for $\text{MnPSe}_{1.32}\text{S}_{1.68}$ can be deduced from the thermal evolution of the circularly polarized Raman spectrum as shown in Fig. 3(f) and Fig. S9 [33]. With increasing temperature toward T_N , the $2M$ excitations in all three compounds soften and broaden rapidly. This behavior contrasts with conventional $2M$ excitations, which persist up to several T_N 's as a form of paramagnons. The strong damping and renormalization are attributed to hybridization with the $S2$ mode, as evinced by the asymmetric line shape of the $S2$ mode. We note that the hybridization of $2M$ with $S1$ is not directly visible; see Fig. 3 and Figs. S7 and S9 [33].

To gain a quantitative insight into the hybridization of the $2M$ excitations with the $S2$ and $S1$ modes, we plot the temperature dependence of their frequency and FWHM in Fig. 4 for $2M$ and $S2$, and Fig. S10 [33] for $S1$ phonon. The hybridization between two quasiparticles manifests through shifts in frequency and linewidth broadening as the phonons' energy and lifetime are renormalized and shortened due to the additional relaxation channels provided by their interaction with $2M$ excitations.

In the case of MnPS_3 , the $S2$ mode shows a softening in frequency below 50 K, accompanying a maximum in FWHM, as indicated by a solid red vertical line in Figs. 4(a) and 4(d). Similarly, the $S1$ mode experiences energy renormalization and line broadening around T_N ; see the red vertical dashed line in Fig. S10 [33]. Above T_N , the FWHM of the $S1$ mode decreases, reaching its minimum at around 100 K. This phenomenon can be rationalized by the interaction between the damped paramagnons in the paramagnetic state and the lower-frequency $S1$ mode, resulting in a wider temperature range of hybridization [48]. Noteworthy is that the enhanced FWHM in the vicinity of the ordered phase is described by

the Lorentzian line shape; see the solid red line in Fig. 4(g) and Fig. S10(g) in the Supplemental Material [33], with peak centers at 52.8 and ~ 79.5 K for $S2$ and $S1$, respectively. Similar anomalies in the frequencies and FWHM of the $S2$ and $S1$ are observed in $\text{MnPSe}_{2.37}\text{S}_{0.63}$, confirming the existence of the same hybridization. In $\text{MnPSe}_{1.32}\text{S}_{1.68}$, the hybridization characteristic remains discernible for the $S2$ mode, while hybridization is not clearly apparent for the $S1$ mode because of the large error bars, which may result from the weak nature of $S1$ and $2M$ excitations.

Next, we attempt to deduce magnetic exchange interactions from the energies of the $2M$ peak based on the expression $\omega_{2m} = J(2zS - 1)$, where ω_{2m} , $S = 5/2$, and $z = 3$ denotes the peak frequency of $2M$, spin number, and the number of nearest-neighbor spins, respectively. These materials comprise three intraplanar exchange coupling parameters: $J1$, $J2$, and $J3$, corresponding to the first, second, and third nearest-neighbor exchange interactions, respectively. While $J1$ and $J3$ possess antiferromagnetic exchange interactions, $J2$ has ferromagnetic interactions; see Fig. S1 in the Supplemental Material [33]. Since the single energy of $2M$ is not sufficient to determine all the magnetic exchange parameters, the determined J should be regarded as a sum of $J1$, $J2$, and $J3$. From the $2M$ peak energies observed at 130.6, 136.9, and 140.7 cm^{-1} for MnPS_3 , $\text{MnPSe}_{2.37}\text{S}_{0.63}$, and $\text{MnPSe}_{1.32}\text{S}_{1.68}$, respectively, J is estimated to be 1.15, 1.20, and 1.24 meV. Overall, the estimated values of J appear somewhat larger than $J(= J1 + J2 + J3) = 0.67 \text{ meV}$ for MnPS_3 and 0.78 meV for $\text{MnPSe}_{1.32}\text{S}_{1.68}$, derived from inelastic neutron scattering [8,49]. This discrepancy arises from the underestimation of $z = 6$ numbers for $J2$ and $J3$. Going from MnPS_3 to MnPS_3 , an increase in exchange interaction is explained by

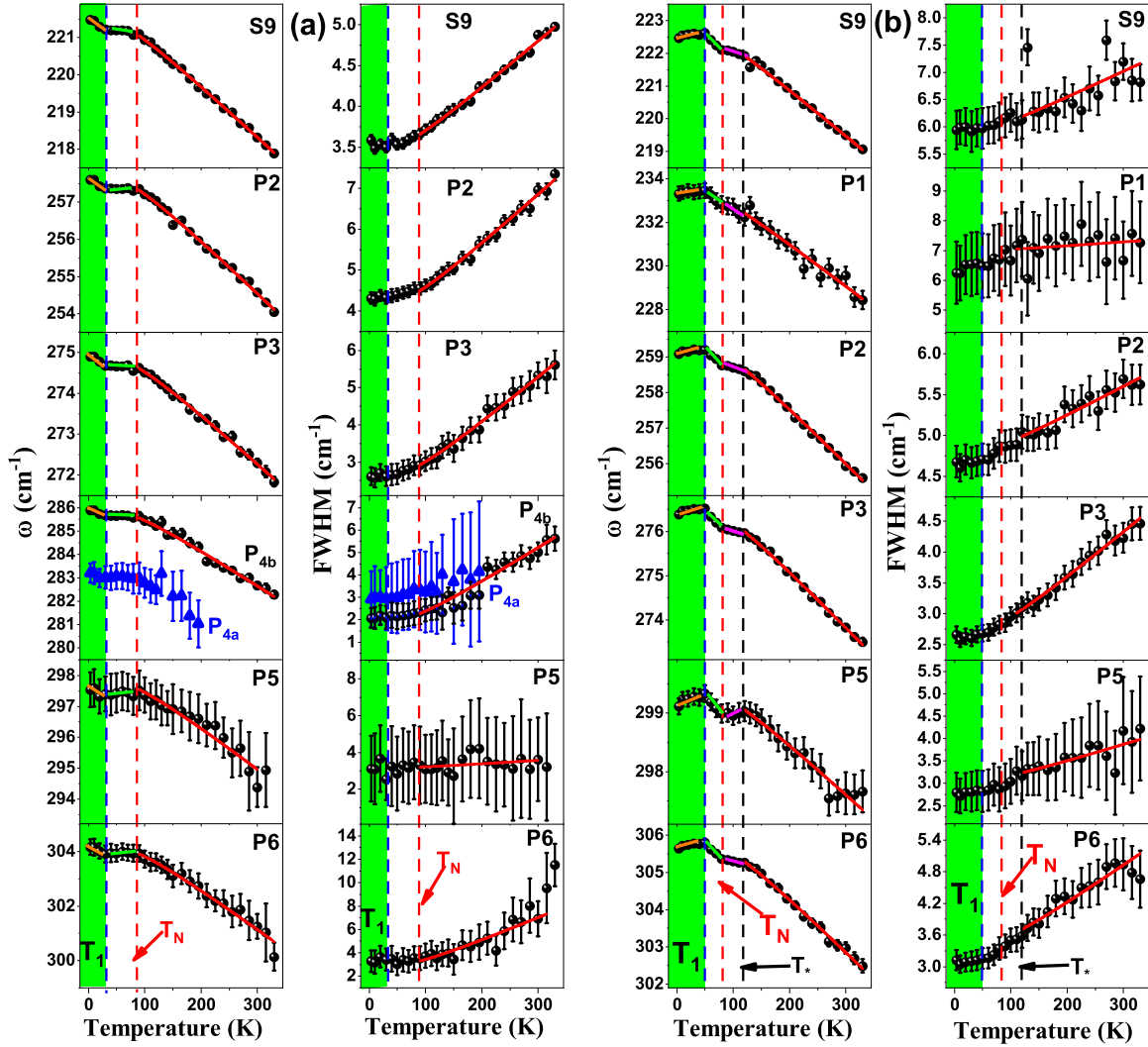


FIG. 5. (a) Temperature-dependent frequency and FWHM of $S9$ and $P2$ – $P6$ for $\text{MnPSe}_{2.37}\text{S}_{0.63}$. (b) Temperature-dependent frequency and FWHM of $S9$ and $P1$ – $P3$, $P5$, and $P6$ for $\text{MnPSe}_{1.32}\text{S}_{1.68}$. The green shaded area shows the topological phase region (T_1). The blue and red dashed lines correspond to the topological phase and antiferromagnetic ordering (T_N) transition temperature, respectively. The black dashed line for the case of $\text{MnPSe}_{1.32}\text{S}_{1.68}$ indicates the presence of the short-range spin-spin corrections. The solid red lines above T_N for $\text{MnPSe}_{2.37}\text{S}_{0.63}$ and T^* for $\text{MnPSe}_{1.32}\text{S}_{1.68}$ are the fitted curves using phonon-phonon anharmonicity interactions as described in the text. The orange, green, and magenta solid lines are guides to the eye. The error bars are the standard error, and were obtained during the extraction of the self-energy parameters using Lorentzian fitting.

the increasing chemical pressure due to the smaller size of S compared to the Se atoms.

C. Emergent multiple phase transitions: Temperature dependence of phonon modes

In the following, we scrutinize the magnetic phase through spin-phonon coupling. Figure 5 illustrates the temperature dependence of frequency and FWHM for several prominent modes: panel (a) $S9$ and $P2$ – $P6$ for $\text{MnPSe}_{2.37}\text{S}_{0.63}$ and panel (b) $S9$, $P1$ – $P3$, $P5$, and $P6$ for $\text{MnPSe}_{1.32}\text{S}_{1.68}$. The low-frequency $S2$ and $S1$ modes are shown in Fig. 4 and Fig. S10 in the Supplemental Material [33] for all three compounds, respectively. Figure S11 shows the temperature-dependent frequency and FWHM of $S3$, $S4$, $S6$, and $S9$ in MnPSe_3 . Additionally, Figs. S12(a) and 12(b), in the Supplemental Material [33], display the temperature-dependent

frequency and FWHM for $S3$, $S4$, and $S6$ of $\text{MnPSe}_{2.37}\text{S}_{0.63}$ and $\text{MnPSe}_{1.32}\text{S}_{1.68}$, respectively.

From Figs. 4 and 5 and Figs. S10–S12 [33], for all three compounds we observed that a phonon softening and broadening above T_N or short-range ordering can be captured within a three-phonon anharmonicity model [50]: $\omega(T) = \omega_0 + A(1 + \frac{2}{e^x - 1})$ and $\Gamma(T) = \Gamma_0 + C(1 + \frac{2}{e^x - 1})$, where $x = \hbar\omega/2k_B T$ and $\omega_0(\Gamma_0)$ represent the frequency (FWHM) of the phonon mode at zero temperature. The coefficients A and C are the cubic-anharmonicity fitting parameters of the three-phonon anharmonicity contributions to $\omega(T)$ and $\Gamma(T)$, respectively. The solid red lines in Figs. 5(a) and 5(b) and Fig. S11 [33] validate the adequacy of our employed model.

Now, we inspect the T dependence of the phonon modes below T_N or the short-ranged ordered phase. From Fig. 4,

and Figs. S10 and S11 in the Supplemental Material [33], for MnPSe_3 the following observations are noteworthy: (i) the frequency of the $S1$ ($S2$) modes softens with decreasing temperature from T_N (~ 50 K) to 40 K (20 K), followed by a slight increase (nearly constant) upon further cooling, (ii) the frequency of the $S3$ mode remains nearly constant, while the frequencies of the $S4$ and $S6$ modes decrease with lowering temperature, (iii) the frequency of $S9$ slightly increases with decreasing temperature, and (iv) the FWHM of the $S1$ and $S2$ modes show a maximum, as discussed in more detail in Sec. III B, while the FWHM of the $S3$, $S4$, $S6$, and $S9$ modes show conventional temperature dependence. The observed anomalies allude to the presence of additional mechanisms.

Within the spin-phonon coupling mechanism, the bare phonon frequency ω_0 is renormalized by spin-spin correlations $\langle S_i S_j \rangle$ between the i th and j th sites of the magnetic ions through spin-phonon coupling λ : $\Delta\omega_{\text{sp-ph}} = \omega_{\text{sp-ph}}(T) - \omega_0 = \lambda \langle \vec{S}_i \cdot \vec{S}_j \rangle$. In the mean-field approximation, we obtain $\langle \vec{S}_i \cdot \vec{S}_j \rangle = -S^2 \phi(T)$, where $\phi(T) = 1 - (T/T_N)^\gamma$ is the order parameter with the critical exponent γ . For 2D magnetic materials like the studied MPX_3 , short-ranged spin-spin correlations survive up to several T_N 's [14,23]. Indeed, the frequency anomalies are discernible up to 80–100 K, see Fig. S11 [33] for certain phonons. The observed anomalous phonon softening on cooling from 100 to ~ 20 K results from the spin-phonon contributions [31]. Remarkably, below ~ 20 K, we further observe a renormalization in the phonon self-energy, clearly visible in both the frequency and FWHM of $S1$ and $S2$, as well as in the intensity of all phonon modes, as depicted in Fig. 4, Fig. 6, and Fig. S10 in the Supplemental Material [33]. Similar anomalies in phonon frequencies are seen for $\text{MnPSe}_{2.37}\text{S}_{0.63}$ ($S9$, and $P2$ – $P6$) and $\text{MnPSe}_{1.32}\text{S}_{1.68}$ ($S9$, $P1$ – $P3$, and $P5$ and $P6$) as well. However, the anomaly is not obvious in the FWHM of the phonon for both $\text{MnPSe}_{2.37}\text{S}_{0.63}$ and $\text{MnPSe}_{1.32}\text{S}_{1.68}$. Instead, the FWHM show continuous narrowing across T_N with a small change in slope, similar to the $S3$, $S4$, $S6$, and $S9$ modes of MnPSe_3 ; see Fig. 5 and Fig. S11 in the Supplemental Material [33].

For $\text{MnPSe}_{2.37}\text{S}_{0.63}$, phonon frequencies show distinct changes in slope with decreasing temperature through ~ 82 – 85 K, suggesting a transition into the long-ranged ordered phase. Intriguingly, upon further cooling within this ordered phase, a noticeable increase in the phonon frequency around 33 K indicates a crossover into another phase, as indicated by the green shaded area in Fig. 5(a). Similarly, for $\text{MnPSe}_{1.32}\text{S}_{1.68}$, the frequency experiences a slope change, while certain modes show a downturn or an upturn at ~ 117 K, signaling that the system enters into a short-range ordered phase. With further lowering temperature below 117 K, we observe another upturn in the frequency around 80 K, followed by a subsequent downturn around 50 K. The successive transitions suggest the onset of yet another phase inside the long-range ordered state; see the green shaded area in Fig. 5(b). The self-energy renormalization as a function of temperature supports the emergence of another phase for all three compounds at ~ 17.5 , ~ 33 , and ~ 50 K below the long-ranged ordered temperatures for MnPSe_3 , $\text{MnPSe}_{2.37}\text{S}_{0.63}$, and $\text{MnPSe}_{1.32}\text{S}_{1.68}$, respectively.

To further confirm the observation of multiple magnetic phase transitions, we measured magnetic susceptibility as a

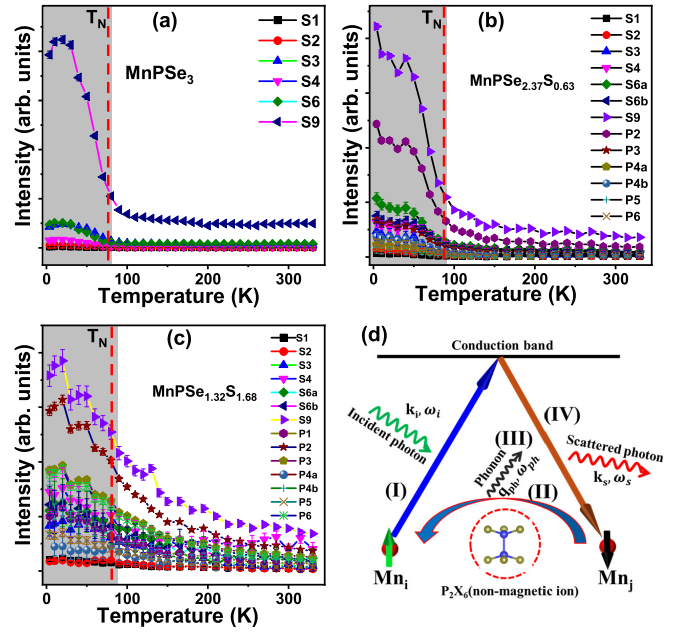


FIG. 6. (a), (b), and (c) Temperature-dependent intensity for some of the selected phonons for MnPSe_3 , $\text{MnPSe}_{2.37}\text{S}_{0.63}$, and $\text{MnPSe}_{1.32}\text{S}_{1.68}$, respectively. The shaded gray area shows the temperature regime where spin-dependent Raman scattering is observed. The red dashed line corresponds to the antiferromagnetic ordering (T_N) transition temperature. (d) Schematic representation of spin-dependent Stokes Raman-scattering process. The error bars are the standard error, and were obtained during the extraction of the self-energy parameters using Lorentzian fitting.

function of temperature for both $\mu_0 H // ab$ (black line in Fig. S14 [33]) and $\mu_0 H // c$ (red line in Fig. S14 [33]) under an external field of 0.02 T. We observe a clear peak centered around ~ 37 K for the case of $\text{MnPSe}_{1.32}\text{S}_{1.68}$, which disappears under a higher magnetic field. For other samples, the secondary phase is not evident due to the low- T Curie tail. Similar anomalous peaks have also been reported in previous magnetic susceptibility [23,51], but their origin is the subject of ongoing investigations.

Here, we recall that the trigonal distortion of MnX_6 octahedra determines a magnetic anisotropy, which modulates spin dimensionality. Both MnPSe_3 and MnPS_3 exhibit XY anisotropy [7,13,52]. A 2D XY system undergoes a topological phase transition, known as the Berezinskii-Kosterlitz-Thouless (BKT) transition, at a finite temperature due to the binding of magnetic vortex–antivortex pairs [53]. The BKT mechanism has been asserted in several MPX_3 members, even in bulk forms [7,52,54]. Nonetheless, the bulk $\text{MnPSe}_{3-x}\text{S}_x$ is known to stabilize a long-range magnetic order thanks to interlayer interactions. We further find no indication that the 2M excitation evolves into topological excitations at the temperatures where the phonon parameters show anomalies; see Fig. 3. Possibly, the subtle trigonal distortion of MnX_6 octahedra might cause spin reorientations by changing the magnetic anisotropy, leading to the renormalization of the phonon self-energy. It should be noted that the sharp increase in magnetic susceptibility observed below the long-range magnetic ordered phase may arise from two sources: (i)

defects and disorder, and (ii) changes in magnetic anisotropy and additional magnetic instabilities. In the former extrinsic case, the phonon's self-energy parameters will remain unaltered. However, in the latter intrinsic case, we expect notable renormalization of the phonon's self-energy parameters. Due to the possible mixture of intrinsic and extrinsic mechanisms, making one-to-one correlations between the phonon anomalies and the susceptibility upturn is not straightforward. Nevertheless, we would like to stress that phonon parameters provide a more powerful means of identifying magnetic instabilities than static magnetic susceptibility in the presence of extrinsic contributions. Future investigations on monolayer $\text{MnPSe}_{3-x}\text{S}_x$ are needed to clarify how the magnetic anomalies evolve to the putative BKT transition in the 2D limit, if present.

D. Tunable spin-dependent Raman scattering

In this section, we address the T -dependent Raman-scattering intensity $I(T)$ of phonons in the magnetically ordered phase. According to the Suzuki and Kamimura (SK) theory, the integrated T -dependent Raman scattering intensity of phonons is given as [55]

$$I(T) = (n + 1) \left[\left| R + M \frac{\langle \vec{S}_i \cdot \vec{S}_j \rangle}{S^2} \right|^2 + |K|^2 \langle S_z^2 \rangle \right], \quad (1)$$

where the term $(n + 1)$ represents the Bose-Einstein factor. The terms associated with the coefficients R and M account for the spin-independent and spin-dependent contribution to $I(T)$, respectively. The last term $K^2 \langle S_z^2 \rangle$, associated with the spins of single ions, could be neglected because its magnitude is two orders of magnitude smaller than that of R and M . Assuming the spin-spin correlations $\langle \vec{S}_i \cdot \vec{S}_j \rangle = -S^2 \phi(T)$, the SK formula is simplified to

$$I(T) = \left| R - M \left[1 - \left(\frac{T}{T_N} \right)^\nu \right] \right|^2. \quad (2)$$

Figures 6(a)–6(c) present the $I(T)$ of selected phonons for $\text{MnPSe}_{3-x}\text{S}_x$ ($x = 0, 0.63, \text{ and } 1.68$). For MnPSe_3 and $\text{MnPSe}_{2.37}\text{S}_{0.63}$, an abrupt decrease in intensity is observed with increasing temperature up to T_N , followed by a slight decrease up to a certain temperature above T_N . With a further increase in temperature, the intensity remains nearly constant. For $\text{MnPSe}_{1.32}\text{S}_{1.68}$, on the other hand, no abrupt change in intensity with temperature takes place. Instead, it shows an exponential decrease with increasing temperature in contrast to MnPSe_3 and $\text{MnPSe}_{2.37}\text{S}_{0.63}$. For MnPSe_3 , the $S1$ and $S2$ modes involving the M^{2+} ions are subject to the modulation of the phonon intensity due to the spin ordering. However, other modes such as $S3, S4, S6, S9$, etc., are associated with the nonmagnetic $(\text{P}_2\text{Se}_6)^{4-}$ clusters and also exhibit similar T -dependent intensity as $S1$ and $S2$. The analogous T -dependent intensities of nonmagnetic and magnetic ion vibrational modes can be understood by considering that the spin-dependent Raman scattering arises from d -electron transfer between magnetic ions through superexchange paths involving nonmagnetic ions.

Figure 6(d) sketches a schematic representation of the spin-dependent Raman-scattering process. Through this

electron-phonon interaction, the spin ordering also has a significant impact on the vibrational modes associated with nonmagnetic ions. In MnPSe_3 , the nonmagnetic $(\text{P}_2\text{Se}_6)^{4-}$ clusters participate in Kramers-Anderson superexchange pathways between neighboring magnetic ions [31,56,57], which explains the T -dependent phonon intensity of $S3, S4, S6$, and $S9$. We note that these modes involve the nonmagnetic $(\text{P}_2\text{Se}_6)^{4-}$ and display similar behavior to $S1$ and $S2$. $\text{MnPSe}_{2.37}\text{S}_{0.63}$ exhibits phonon intensity behavior, akin to MnPSe_3 . However, the T -dependent intensity trend for $\text{MnPSe}_{1.32}\text{S}_{1.68}$ differs markedly, displaying a nearly exponential behavior rather than the abrupt change observed in MnPSe_3 and $\text{MnPSe}_{2.37}\text{S}_{0.63}$. This suggests a weakening of spin-dependent Raman scattering in $\text{MnPSe}_{1.32}\text{S}_{1.68}$.

For quantitative analysis, we fitted normalized $I(T)$ of the intense phonon modes to Eq. (2) in the magnetically ordered phase; see Fig. S15 and Table S3 in the Supplemental Material [33] for the fitting parameters. The spin-independent R term increases, while the spin-independent M term decreases with increasing S concentration, indicating a weakening in the spin-dependent Raman scattering. Variations in spin-dependent Raman scattering have also been reported as a function of temperature and composition [17]. The weakening or diminishing of the spin-dependent Raman scattering in $\text{MnPSe}_{1.32}\text{S}_{1.68}$ may result from enhanced chemical disorder and the presence of competing exchange interactions through $(\text{P}_2(\text{Se}_{1-x}\text{S}_x)_6)^{4-}$ clusters. We note that the parent compounds MnPSe_3 and MnPS_3 exhibit the in-plane and out-of-plane spin alignments, respectively. Consequently, in $\text{MnPSe}_{1.32}\text{S}_{1.68}$ two superexchange processes become frustrated, destructively interfering between two competing spin-dependent scattering processes.

IV. CONCLUSION

In summary, we have reported a detailed Raman-scattering study of $\text{MnPSe}_{3-x}\text{S}_x$ ($x = 0, 0.63, \text{ and } 1.68$) to understand the intricate confluence of lattice and magnetic excitations as functions of temperature and chemical composition. Probing two-magnon excitations across all investigated compounds reveals that the strength of their hybridization with $S2$ to $S1$ phonon modes is notably affected by chalcogen substitution. Through Raman spectroscopy and magnetic susceptibility measurements, we identify a sequence of three-phase transitions with decreasing temperature: short- and long-range magnetically ordered phases, and a distinct low-temperature phase inside the long-range ordered state, associated with spin reorientations or magnetic instabilities inherent to two-dimensional topological state. We further find the significant role of spin dynamics and the Kramers-Anderson superexchange pathways in modulating spin-dependent phonon-scattering intensities. Our work demonstrates the potential of chalcogen substitution as a tool for tailoring their magnetic and lattice characteristics as well as their mutual coupling through engineering $(\text{P}_2(\text{Se}_{1-x}\text{S}_x)_6)^{4-}$ clusters.

ACKNOWLEDGMENTS

This work was supported by the National Research Foundation (NRF) of Korea (Grants No. 2020R1A5A1016518, No. 2022R1A2C1003959, and No. RS-2023–00209121). R.S.

acknowledges the financial support provided by the Ministry of Science and Technology in Taiwan under Projects No. NSTC 11–2124-M-001–007, No. NSTC 113–2112-M-

001-045-MY3, and No. NSTC111-2124-M-A49-009 and Academia Sinica for the budget of Grant No. AS-iMATE-113–12.

- [1] N. D. Mermin and H. Wagner, Absence of ferromagnetism or antiferromagnetism in one- or two-dimensional isotropic Heisenberg models, *Phys. Rev. Lett.* **17**, 1133 (1966).
- [2] B. Huang, G. Clark, E. N. Moratalla, D. R. Klein, R. Cheng, K. L. Seyler, D. Zhong, E. Schmidgall, M. A. McGuire, D. H. Cobden, W. Yao, D. Xiao, P. J. Herrero, and X. Xu, Layer-dependent ferromagnetism in a van der Waals crystal down to the monolayer limit, *Nature (London)* **546**, 270 (2017).
- [3] C. Gong, L. Li, Z. Li, H. Ji, A. Stern, Y. Xia, T. Cao, W. Bao, C. Wang, Y. Wang, Z. Q. Qiu, R. J. Cava, S. G. Louie, J. Xia, and Xiang Zhang, Discovery of intrinsic ferromagnetism in two-dimensional van der Waals crystals, *Nature (London)* **546**, 265 (2017).
- [4] X. Jiang, Q. Liu, J. Xing, N. Liu, Y. Guo, Z. Liu, and J. Zhao, Recent progress on 2D magnets: Fundamental mechanism, structural design and modification, *Appl. Phys. Rev.* **8**, 031305 (2021).
- [5] Q. H. Wang, A. B. Pinto, M. Blei, A. H. Dismukes, A. Hamo, S. Jenkins, M. Koperski, Y. Liu, Q. C. Sun, E. J. Telford *et al.*, The magnetic genome of two-dimensional van der waals materials, *ACS Nano* **16**, 6960 (2021).
- [6] J. U. Lee, S. Lee, J. H. Ryoo, S. Kang, T. Y. Kim, P. Kim, C. H. Park, J. G. Park, and H. Cheong, Ising-type magnetic ordering in atomically thin FePS₃, *Nano Lett.* **16**, 7433 (2016).
- [7] S. Chaudhuri, C. N. Kuo, Y. S. Chen, C. S. Lue, and J. G. Lin, Low-temperature magnetic order rearrangement in the layered van der Waals compound MnPS₃, *Phys. Rev. B* **106**, 094416 (2022).
- [8] S. Calder, A. V. Haglund, A. I. Kolesnikov, and D. Mandrus, Magnetic exchange interactions in the van der Waals layered antiferromagnet MnPSe₃, *Phys. Rev. B* **103**, 024414 (2021).
- [9] K. Kim, S. Y. Lim, J. U. Lee, S. Lee, T. Y. Kim, K. Park, G. S. Jeon, C. H. Park, J. G. Park, and H. Cheong, Suppression of magnetic ordering in XXZ-type antiferromagnetic monolayer NiPS₃, *Nat. Commun.* **10**, 345 (2019).
- [10] P. A. Joy and S. Vasudevan, Magnetism in the layered transition-metal thiophosphates MPS₃ (M = Mn, Fe, and Ni), *Phys. Rev. B* **46**, 5425 (1992).
- [11] S. Selter, Y. Shemerliuk, M. I. Sturza, A. U. B. Wolter, B. Büchner, and S. Aswartham, Crystal growth and anisotropic magnetic properties of quasi-two-dimensional (Fe_{1-x}Ni_x)₂P₂S₆, *Phys. Rev. Mater.* **5**, 073401 (2021).
- [12] D. Lançon, H. C. Walker, E. Ressouche, B. Ouladdiaf, K. C. Rule, G. J. McIntyre, T. J. Hicks, H. M. Rønnow, and A. R. Wildes, Magnetic structure and magnon dynamics of the quasi-two-dimensional antiferromagnet FePS₃, *Phys. Rev. B* **94**, 214407 (2016).
- [13] P. Jeevanandam and S. Vasudevan, Magnetism in MnPSe₃: A layered 3d⁵ antiferromagnet with unusually large XY anisotropy, *J. Phys.: Condens. Matter* **11**, 3563 (1999).
- [14] A. Bhutani, J. L. Zuo, R. D. McAuliffe, C. R. dela Cruz, and D. P. Shoemaker, Strong anisotropy in the mixed antiferromagnetic system Mn_{1-x}Fe_xPSe₃, *Phys. Rev. Mater.* **4**, 034411 (2020).
- [15] J. N. Graham, M. J. Coak, S. Son, E. Suard, J. G. Park, L. Clark, and A. R. Wildes, Local nuclear and magnetic order in the two-dimensional spin glass Mn_{0.5}Fe_{0.5}PS₃, *Phys. Rev. Mater.* **4**, 084401 (2020).
- [16] R. Basnet, A. Wegner, K. Pandey, S. Storment, and J. Hu, Highly sensitive spin-flop transition in antiferromagnetic van der Waals material MPS₃ (M = Ni and Mn), *Phys. Rev. Mater.* **5**, 064413 (2021).
- [17] S. Lee, J. Park, Y. Choi, K. Raju, W. T. Chen, R. Sankar, and K. Y. Choi, Chemical tuning of magnetic anisotropy and correlations in Ni_{1-x}Fe_xPS₃, *Phys. Rev. B* **104**, 174412 (2021).
- [18] N. Chandrasekharan and S. Vasudevan, Dilution of a layered antiferromagnet: Magnetism, *Phys. Rev. B* **54**, 14903 (1996).
- [19] V. Manrí, P. Barahona, and O. Pen, Physical properties of the cation-mixed M'MPS₃ phases, *Mater. Res. Bull.* **35**, 1889 (2000).
- [20] F. Wang, N. Mathur, A. N. Janes, H. Sheng, P. He, X. Zheng, P. Yu, A. J. DeRuiter, J. R. Schmidt, J. He, and S. Jin, Defect-mediated ferromagnetism in correlated two-dimensional transition metal phosphorus trisulfides, *Sci. Adv.* **7**, eabj4086 (2021).
- [21] N. Khan, D. Kumar, V. Kumar, Y. Shemerliuk, S. Selter, B. Büchner, K. Pal, S. Aswartham, and P. Kumar, Interplay of topology and antiferromagnetic order in two-dimensional van der Waals crystals of (Ni_xFe_{1-x})₂P₂S₆, *2D Mater.* **11**, 035018 (2024).
- [22] R. Basnet, K. M. Kotur, M. Rybak, C. Stephenson, S. Bishop, C. Autieri, M. Birowska, and J. Hu, Controlling magnetic exchange and anisotropy by nonmagnetic ligand substitution in layered MPX₃ (M = Ni, Mn; X = S, Se), *Phys. Rev. Res.* **4**, 023256 (2022).
- [23] H. Han, H. Lin, W. Gan, Y. Liu, R. Xiao, L. Zhang, Y. Li, C. Zhang, and H. Li, Emergent mixed antiferromagnetic state in MnPS_{3(1-x)}Se_{3x}, *Appl. Phys. Lett.* **122**, 033101 (2023).
- [24] T. T. Mai, K. F. Garrity, A. McCreary, J. Argo, J. R. Simpson, V. Doan-Nguyen, R. V. Aguilar, and A. R. Hight Walker, Magnon-phonon hybridization in 2D antiferromagnet MnPSe₃, *Sci. Adv.* **7**, eabj3106 (2021).
- [25] S. Liu, A. Granados del Águila, D. Bhowmick, C. K. Gan, T. Thu Ha Do, M. A. Prosnikov, D. Sedmidubský, Z. Sofer, P. C. M. Christianen, P. Sengupta, and Q. Xiong, Direct observation of magnon-phonon strong coupling in two-dimensional antiferromagnet at high magnetic fields, *Phys. Rev. Lett.* **127**, 097401 (2021).
- [26] D. Jana, P. Kapuscinski, I. Mohelsky, D. Vaclavkova, I. Breslavetz, M. Orlita, C. Faugeras, and M. Potemski, Magnon gap excitations and spin-entangled optical transition in the van der Waals antiferromagnet NiPS₃, *Phys. Rev. B* **108**, 115149 (2023).
- [27] J. Luo, S. Li, Z. Ye, R. Xu, H. Yan, J. Zhang, G. Ye, L. Chen, D. Hu, X. Teng, W. A. Smith, B. I. Yakobson, P. Dai, A. H. Nevidomskyy, R. He, and H. Zhu, Evidence for topological magnon-phonon hybridization in a 2D antiferromagnet down to the monolayer limit, *Nano Lett.* **23**, 2023 (2023).

- [28] A. McCreary, J. R. Simpson, T. T. Mai, R. D. McMichael, J. E. Douglas, N. Butch, C. Dennis, R. Valdés Aguilar, and A. R. Hight Walker, Quasi-two-dimensional magnon identification in antiferromagnetic FePS₃ via magneto-Raman spectroscopy, *Phys. Rev. B* **101**, 064416 (2020).
- [29] X. Hou, X. Zhang, Q. Ma, X. Tang, Q. Hao, Y. Cheng, and T. Qiu, Alloy engineering in few-layer manganese phosphorus trichalcogenides for surface-enhanced Raman scattering, *Adv. Funct. Mater.* **30**, 191171 (2020).
- [30] V. Kumar, D. Kumar, B. Singh, Y. Shemerliuk, M. Behnami, B. Büchner, S. Aswartham, and P. Kumar, Fluctuating fractionalized spins in quasi-two-dimensional magnetic V_{0.85}PS₃, *Phys. Rev. B* **107**, 094417 (2023).
- [31] D. J. Gillard, D. Wolverson, O. M. Hutchings, and A. I. Tartakovskii, Spin-order-dependent magneto-elastic coupling in two dimensional antiferromagnetic MnPSe₃ observed through Raman spectroscopy, *Npj 2D Mater. Appl.* **8**, 6 (2024).
- [32] Y. J. Sun, Q. H. Tan, X. L. Liu, Y. F. Gao, and J. Zhang, Probing the magnetic ordering of antiferromagnetic MnPS₃ by Raman spectroscopy, *J. Phys. Chem. Lett.* **10**, 3087 (2019).
- [33] See Supplemental Material at <http://link.aps.org/supplemental/10.1103/PhysRevB.110.064414> for crystal and magnetic structures, details about expected phonon excitations, selection rules for circularly polarized Raman scattering, additional figures and tables as well as magnetic susceptibility, XRD and EDX data, and which includes Refs. [8,22,34,38,39,58–61].
- [34] M. Chisa, S. Tomoyuki, T. Yoshiko, and K. Koh, Raman scattering in the two-dimensional antiferromagnet MnPSe₃, *J. Phys.: Condens. Matter* **5**, 623 (1993).
- [35] P. Liu, Z. Xu, H. Huang, J. Li, C. Feng, M. Huang, M. Zhu, Z. Wang, Z. Zhang, D. Hou, Y. Lu, and B. Xiang, Exploring the magnetic ordering in atomically thin antiferromagnetic MnPSe₃ by Raman spectroscopy, *J. Alloys Compd.* **828**, 154432 (2020).
- [36] M. Bernasconi, G. L. Marra, G. Benedek, L. Miglio, M. Jouanne, C. Julien, M. Scagliotti, and M. Balkanski, Lattice dynamics of layered MPX₃ (M = Mn, Fe, Ni, Zn; X = S, Se) compounds, *Phys. Rev. B* **38**, 12089 (1988).
- [37] J. Qiu, W. J. Huang, Y. J. Lee, S. Kim, X. B. Chen, and I. S. Yang, Raman study of the spin–lattice excitations of the layered antiferromagnets MPSe₃ (M = Fe, Mn), *Results Phys.* **56**, 107256 (2024).
- [38] A. Hashemi, H. P. Komsa, M. Puska, and A. V. Krasheninnikov, Vibrational properties of metal phosphorus trichalcogenides from first-principles calculations, *J. Phys. Chem. C* **121**, 27207 (2017).
- [39] K. Kim, S. Y. Lim, J. Kim, J. U. Lee, S. Lee, P. Kim, K. Park, S. Son, C. H. Park, and J. G. Park, Antiferromagnetic ordering in van der Waals 2D magnetic material MnPS₃ probed by Raman spectroscopy, *2D Mater.* **6**, 041001 (2019).
- [40] D. Vaclavkova, A. Delhomme, C. Faugeras, M. Potemski, A. Bogucki, J. Suffczyński, P. Kossacki, A. R. Wildes, B. Grémaud, and A. Saúl, Magnetoelastic interaction in the two-dimensional magnetic material MnPS₃ studied by first principles calculations and Raman experiments, *2D Mater.* **7**, 035030 (2020).
- [41] R. Oliva, E. Ritov, F. Horani, I. Etxebarria, A. K. Budniak, Y. Amoyal, E. Lifshitz, and M. Guennou, Lattice dynamics and in-plane antiferromagnetism in Mn_xZn_{1-x}PS₃ across the entire composition range, *Phys. Rev. B* **107**, 104415 (2023).
- [42] M. Balkanski, M. Jouanne, G. Ouvrard, and M. Scagliotti, Effects due to spin ordering in layered MPX₃ compounds revealed by inelastic light scattering, *J. Phys. C: Solid State Phys.* **20**, 4397 (1987).
- [43] G. Güntherodt, Light scattering in magnetic semiconductors, *J. Magn. Magn. Mater.* **11**, 394 (1979).
- [44] M. Balkanski, K. P. Jain, R. Beserman, and M. Jouanne, Theory of interference distortion of Raman scattering line shapes in semiconductors, *Phys. Rev. B* **12**, 4328 (1975).
- [45] R. Loudon, The Raman effect in crystals, *Adv. Phys.* **50**, 813 (2001).
- [46] P. A. Fleury and R. Loudon, Scattering of light by one- and two-magnon excitations, *Phys. Rev.* **166**, 514 (1968).
- [47] P. A. Fleury, S. P. S. Porto, and R. Loudon, Two-magnon light scattering in antiferromagnetic MnF₂, *Phys. Rev. Lett.* **18**, 658 (1967).
- [48] P. A. Fleury, Paramagnetic spin waves and correlation functions in NiF₂, *Phys. Rev.* **180**, 591 (1969).
- [49] R. Baral, A. V. Haglund, J. Liu, A. I. Kolesnikov, D. Mandrus, and S. Calder, Local spin structure in the layered van der Waals materials MnPS_xSe_{3-x}, *Phys. Rev. B* **110**, 014423 (2024).
- [50] P. G. Klemens, Anharmonic decay of optical phonon in diamond, *Phys. Rev. B* **11**, 3206 (1975).
- [51] X. Yan, X. Chen, and J. Qin, Synthesis and magnetic properties of layered MnPS_xSe_{3-x} (0 < x < 3) and corresponding intercalation compounds of 2,2'-Bipyridine, *Mater. Res. Bull.* **46**, 235 (2011).
- [52] A. R. Wildes, H. M. Rønnow, B. Roessli, M. J. Harris, and K. W. Godfrey, Static and dynamic critical properties of the quasi-two-dimensional antiferromagnet MnPS₃, *Phys. Rev. B* **74**, 094422 (2006).
- [53] J. M. Kosterlitz and D. J. Thouless, Ordering, metastability and phase transitions in two-dimensional systems, *J. Phys. C: Solid State Phys.* **6**, 1181 (1973).
- [54] G. Liao, S. Zhang, P. Cui, and Z. Zhang, Tunable Meron pair excitations and Berezinskii-Kosterlitz-Thouless phase transitions in the monolayer antiferromagnet MnPS₃, *Phys. Rev. B* **109**, L100403 (2024).
- [55] N. Suzuki and H. Kamimura, Theory of spin-dependent phonon Raman scattering in magnetic crystals, *J. Phys. Soc. Jpn.* **35**, 985 (1973).
- [56] P. W. Anderson, Antiferromagnetism. theory of superexchange interaction, *Phys. Rev.* **79**, 350 (1950).
- [57] H. A. Kramers, L'interaction entre les atomes magnétogènes dans un cristal paramagnétique, *Physica* **1**, 182 (1934).
- [58] K. Momma and F. Izumi, VESTA 3 for three-dimensional visualization of crystal, volumetric and morphology data, *J. Appl. Crystallogr.* **44**, 1272 (2011).
- [59] S. Yan, W. Wang, C. Wang, L. Chen, X. Ai, Q. Xie, and G. Cheng, Anharmonic phonon scattering study in MnPS₃ crystal by Raman spectroscopy, *Appl. Phys. Lett.* **121**, 032203 (2022).
- [60] W. Hayes and R. Loudon, *Scattering of Light by Crystals* (John Wiley and Sons, New York, 1978).
- [61] M. Cardona and G. Güntherodt, *Light Scattering in Solid II* (Springer, Berlin, 1982).